


RESEARCH

Open Access



Chemical and isotopic constraints on fluid origin and genesis of geothermal systems in the Tingri-Tangra Yumco rift, southern Tibetan Plateau

Wei Liu^{1,2}, Maoliang Zhang^{2*} , Yi Liu², Lifeng Cui², Yuji Sano³ and Sheng Xu^{2*}

*Correspondence:
mzhang@tju.edu.cn; sheng.xu@tju.edu.cn

¹ Key Laboratory of Environmental Pollution Control and Remediation at Universities of Inner Mongolia Autonomous Region, College of Resources and Environmental Engineering, Inner Mongolia University of Technology, Hohhot 010051, China

² Institute of Surface-Earth System Science, School of Earth System Science, Tianjin University, Tianjin 300072, China

³ Marine Core Research Institute, Kochi University, Kochi 783-8502, Japan

Abstract

Numerous geothermal systems are hosted by extensional rifts that transect the Himalayas and Lhasa block in the Himalayan–Tibetan orogen. However, the relationships between hydrogeological processes and geothermal fluid circulation in different tectonic units remain unclear. Here, we report an integrated dataset of chemical and isotopic compositions (including major and trace elements, δD , $\delta^{18}O$, and $^{87}Sr/^{86}Sr$) of thermal spring water from the Tingri-Tangra Yumco rift to assess their origins and circulation processes. $\delta^{18}O$ (–21.3 to –17.0‰) and δD (–166 to –135‰) values of thermal springs indicate dominant recharge of meteoric waters from areas with elevation of > 6000 m and minor addition of magmatic fluids. Meteoric water could infiltrate to depths of about 1700–2900 m along the faults, whereby it is influenced by geothermal gradient and/or conductive heat transfer of magmatic fluids. The thermal spring waters are mainly Na–HCO₃ type and are controlled by dissolution of silicate and carbonate minerals and mixing with deep fluids. The results of chemical and multicomponent geothermometers indicate reservoir temperatures of 115–195 °C, corresponding to a convection heat flux of 3.96×10^5 J/s to 1.78×10^7 J/s from geothermal systems, which are comparable to that of the low-enthalpy geothermal systems in southern Italy. Geochemical modeling is conducted to assess the water–mineral equilibria in the reservoir. Trace elements and $^{87}Sr/^{86}Sr$ data suggest spatially variable controlling factors for the rift-related geothermal systems: (1) interaction with granitoid and carbonate in the Himalayas; (2) cold groundwater mixing with that leaching from granite and volcanic rocks in the Lhasa block; (3) the input of vapors from magmatic degassing. The geochemistry of thermal springs associated with extensional rift is largely induced by the interaction between fluid and different reservoir rocks in the Himalayas and Lhasa block. Based on these findings, a genetic model is proposed for exploration and development of geothermal resources in the Tingri-Tangra Yumco rift.

Keywords: Geothermal fluids, Hydrochemistry, Stable isotopes, Geothermometry, Tingri-Tangra Yumco rift, Himalayan–Tibetan orogen

Introduction

Geothermal systems represent one of the most obvious manifestations of energy-releasing from Earth's interior. The emergence of hydrothermal activities (e.g., hot and boiling springs) at the surface is generally controlled by the networks of faults or fractures, which generate high permeability and porosity for the uprising of groundwater and/or deeply derived fluids (Egger et al. 2014; Rowland et al. 2008). At a global scale, the first-order control on distribution of Earth's geothermal energy resources is the plate tectonic movement. Particularly, geothermal systems are abundant in regions where two plates converge (e.g., subduction zones and collisional orogens) due to intensive tectonic and volcanic activities (Barde-Cabusson et al. 2009; Newell et al. 2008; Scott et al. 2020).

The Himalayan–Tibetan orogen (HTO) is one of the largest active convergent plate margins on Earth, resulting from collision between the Indian and Asian continents since early Cenozoic (Yin and Harrison 2000). A significant geological feature of the HTO is the seven large-scale near N–S trending extensional rifts that extend from the Himalayas in the south to the Lhasa block in the north (Fig. 1; Kapp and Decelles 2019). Previous geological and geophysical investigations revealed that these rift systems are accompanied by intense hydrothermal activities (e.g., thermal springs, boiling springs, geysers, and fumaroles) and high heat flow values (Jiang et al. 2019; Klemperer et al. 2022; Tong et al. 2000), suggesting the importance of geothermal energy resources in the HTO. Most studies focus on geochemistry and geothermometry of thermal springs from several high-temperature geothermal fields (e.g., Yangbajing and Gudui) that have been exploited in the rifts (Wang et al. 2020, 2022; Yuan et al. 2014; Zhao et al. 1998). However, less attention has been given to rift-scale investigation on the origin and circulation path, and water–rock interaction processes of hydrothermal fluids (Zhou et al. 2023), which also discourages further evaluation and exploitation of geothermal resources in the HTO.

Our study area, the Tingri-Tangra Yumco rift (TTYR; Fig. 1), is one of the most typical extensional rift systems of the Tibetan Plateau, where tens of geothermal fields are scattered along the rift and K-rich volcanic rocks (e.g., leucite phonolite, tephrite and trachyandesite) were formed between 25 and 8 Ma (Guo et al. 2015; Tong et al. 2000). It is a potentially important rift zone for geothermal energy (Wang et al. 2017), but only two thermal springs in the Tingri area of the TTYR have been studied for hydrogeological and geochemical characteristics (Newell et al. 2008). The genesis of geothermal systems in the TTYR remains unclear; and especially, few detailed previous investigations on the hydrogeological settings, geochemical processes, and the genetic mechanism of geothermal systems have been carried out in the TTYR.

Here, we present a detailed chemical and isotopic dataset from thermal springs along the TTYR. The goal of this study is (i) to identify the chemical type and source of geothermal fluid; (ii) to characterize water–rock interaction; (iii) to assess the temperature of a potential geothermal reservoir; and (iv) to discuss the relationship between tectonic activity and fluid migration. Finally, a conceptual model of the geothermal system that incorporates the main geological-structural features of the area is presented.

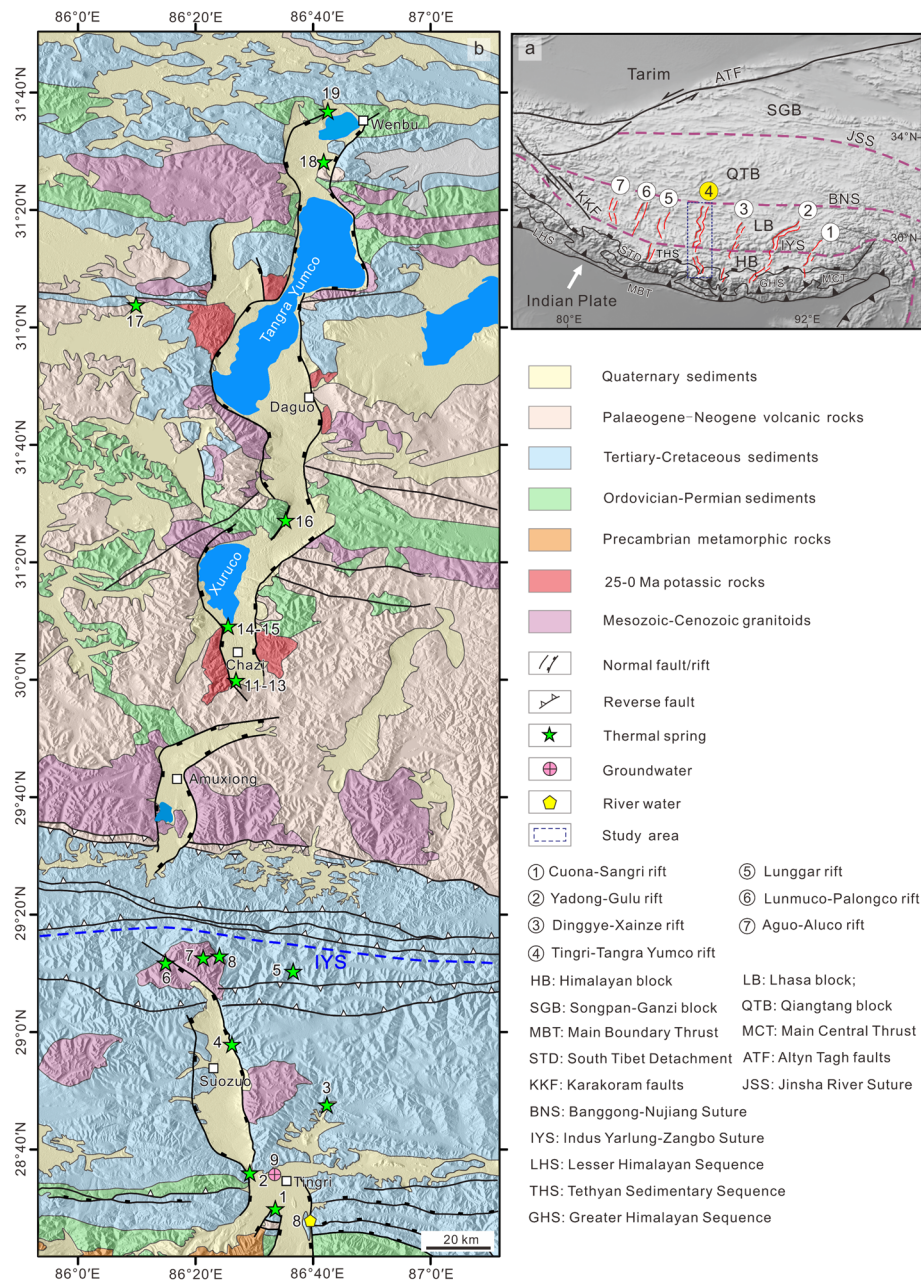


Fig. 1 Geological setting of the geothermal system along the TTYR: **a** Map showing the location of the TTYR with the green line in the HTO. **b** Geological map of the TTYR and distribution of thermal springs. The number of thermal springs is listed in Table 1

Geologic and hydrogeologic background

Geological setting

HTO formed by the India–Asia collision consists of several continental terranes progressively accreted at the southern margin of Eurasia during the Mesozoic and Cenozoic (Yin and Harrison 2000). These terranes are separated by Jinsha, Bangong-Nujiang, and Indus-Yarlung suture (IYS) zone from north to south (Fig. 1). India–Asia collision resulted in widespread crustal north–south shortening and east–west extension, and

intense metamorphism and magmatism along the orogen (Hodges 2000; Yin and Harrison 2000). The E–W extension of the Tibetan Plateau is markedly characterized by a series of N–S trending rift valley systems between the Himalayas and the BNS that are possibly driven by orogenic collapse, delamination of mantle lithosphere, large-scale eastward extrusion of Tibetan lithosphere, northward underthrusting of the Indian slab (Sundell et al. 2013 and references therein). Several extensional rifts composed of numerous active normal faults cut the Himalayas, Lhasa block, and IYS. A large-scale focal zone of hydrothermal activities appears along these rifts and is consistent with the high heat flow values of the India–Asia collision zone (Zhang et al. 2021 and references therein).

The N–S trending TTYR is approximately 400 km in length, extends across southern Tibet into the Himalayas, crosscutting the IYS, and is one of the most typical Tibetan rifts (Fig. 1). Miocene potassic to ultrapotassic volcanism is recorded along northern TTYR (Zhao et al. 2022). The southern TTYR located in the Himalayas, near the old Tingri region, is composed of Tingri graben in the Tethyan Himalayan zone that is filled by Quaternary outwash from the north side of the Himalaya. The Tethyan Himalayan zone contains deformed passive margin sediments dominated by carbonates with subordinate volcanic and clastic rocks (Parsons et al. 2020 and references therein) and is separated from the Greater Himalayan zone along the South Tibet Detachment System (STDS). The Greater Himalayan zone, beneath the STDS, consists of metasedimentary, metavolcanic rocks and Eocene–Miocene granitic intrusions (van Hinsbergen et al. 2019 and references therein). The 300-km-long northern TTYR distributed in the Lhasa block is mainly made up of the Xuruco graben and Tangra Yumco graben, which is bounded on both the east and west by nearly parallel N–S striking active normal faults. These faults display the large scarps along the range front and locally show extremely high triangular facets, which are visible on satellite imagery and in the field. Ultra-potassic volcanic rocks between 25 and 8 Ma are present along the N–S trending faults (Guo et al. 2015). The outcropped rocks involve volcanic and clastic rock, granites, and Quaternary alluvium within the graben.

Hydrothermal manifestations

Hydrothermal activity occurs throughout the TTYR and is marked by hot springs, boiling springs, geysers, and steam fissures. Thermal springs are spatially distributed along N–S trending faults on both sides of the TTYR. The temperature of spring substantially higher than the annual average temperature of 5 °C can be called thermal springs at Tibet Plateau (Tong et al. 2000). The hot springs are natural circular pools and/or artificial pools, several centimeters to meters in diameter (Fig. 2a–d). The thermal springs present intense gas bubbling within the pools (Liu et al. 2024) and around hydrothermal altered ground (e.g., salts, silica residue, clays, and native sulphur). The various scale of travertine deposition is observed around thermal springheads except for the Kajiu spring, Chazi spring, and Dangqiong spring (Fig. 2c, d). Where outcropped, travertine depositions commonly appear as fissure-ridge and spring-mound. The striking fissure ridges at some springs (e.g., Camuda spring, Gongbasaba spring and Yundong spring) are aligned parallel to the N–S strike of the normal faults (Newell et al. 2008). The chemical and isotopic composition of some hydrothermal gases was reported by some studies



Fig. 2 Field observation of thermal springs and travertine deposits along the TTYR. **a** Natural circular pools of Gongbasaba springs have numerous gas bubbling; **b** spring outlet and hydrothermal alteration material distributed along the N–S trending fissure ridge in Gongbasaba geothermal field. **c** 3.5 m-high travertine mounds in Yundong geothermal field; **d** Boiling water in pools of Chazi spring

(Klemperer et al. 2022; Newell et al. 2008; Zhao et al. 2022). Thermal waters flow to the outside of pools through one or more shallow discharge channels along the slope of mounds.

Materials and methods

Water sampling and analysis

Several datasets of thermal springs in Himalayan block from sampling campaigns by Tong et al. (2000) and Newell et al. (2008), are selected for this study. A total of 16 water samples (14 thermal springs, 1 river and 1 well water) are sampled along the Tingri-Tangra Yumco rift in May–July 2021. Parameters such as temperature, pH and electrical conductivity (EC) were determined in the field using a portable multi-parameter device (WTW Multi 3630 IDS, Germany) with a resolution of 0.1 °C, 0.01 and 1 $\mu\text{S}/\text{cm}$, respectively. For major ion analysis, water samples were filtered using a 0.45- μm pore-size membrane filter into high-density polypropylene bottles. Filtered water samples were collected in 100-ml glass bottles for oxygen and hydrogen isotopic analyses. Samples were acidized with trace-metal grade HNO_3 to $\text{pH} < 2$ to analyze the content of trace elements and Sr isotopic composition.

The HCO_3^- and CO_3^{2-} concentration was determined in the field by titration with HCl (0.02 mol/L), using phenolphthalein and methyl-orange as indicators. Major cation (Na^+ , K^+ , Ca^{2+} and Mg^{2+}) and anion (Cl^- , SO_4^{2-} and F^-) concentrations were determined by ion chromatography (Thermo Fisher, ICS-Aquion 1100). The errors of the water chemical composition assessed by anion–cation charge balance are below 5% for

most water samples (Table 2). The concentrations of selected trace elements (Li, B, Rb, Cs and Sr) were analyzed by inductively coupled plasma mass spectrometer (Agilent 7900, USA). Dissolved SiO₂ was analyzed by a Skalar San Plus autoanalyzer (San ++, SKALAR Corp., The Netherlands).

The hydrogen and oxygen isotopes were determined by a high-precision water isotope analyzer (Picarro L2140-i, USA) with an analytical uncertainty of $\pm 0.3\%$ and $\pm 1\%$, respectively. The results were expressed in δ -per mil (‰) relative to the Vienna Standard Mean Ocean Water (V-SMOW). Strontium was separated from water samples by using the cation exchange column (AG500W-X8, 200–400 mesh). In this study, the global meteoric water line (GMWL) is typically defined by the following equation (Craig 1961): $\delta D = 8\delta^{18}O + 10$. The local meteoric water line (LMWL) is represented by $\delta D = 8.2\delta^{18}O + 14.4$ (Tan et al. 2014).

The ⁸⁷Sr/⁸⁶Sr of water samples were analyzed by multi-receiver inductively coupled plasma mass spectrometer (Nu Plasma I, Nu Instruments, UK) with the NBS SRM987 with ⁸⁷Sr/⁸⁶Sr of 0.71030 ± 2 (2SD, n = 19) as the bracketing standard. These analyses were carried out in School of Earth System Science at Tianjin University.

Recharge elevations calculation

The O and H isotopic compositions of thermal waters are commonly used as tracers for determining the recharge elevations of waters (Clark and Fritz 1997). Considering the presence of $\delta^{18}O$ shift in the high-temperature geothermal field, δD values are only minimally affected leading to near-horizontal trends to the right of GMWL (Liu et al. 2022 and references therein) and used to more accurately calculate the recharge elevation of thermal springs (Li et al. 2020). Accordingly, an equation for the recharge elevations of geothermal water is proposed as below:

$$H_{Alt} = \frac{\delta G_w - \delta R_w}{f} + h, \quad (1)$$

where H_{Alt} denotes the recharge elevation in m.a.s.l, δG_w is the value of δD for sampled thermal water, δR_w is the δD value for the surface water (-135% in this study), f is an altitude gradient of δD values for the meteoric water ($-2.6\%/100$ m in the eastern Tibetan Plateau, Yu et al. 1984), h is the altitude of samples.

Geothermometry and geothermometric modeling

Geothermometers are utilized to estimate the reservoir temperature of thermal fluid at depth, which is cost-effective method in geothermal exploration. Chemical geothermometry is the most common way to estimate the subsurface temperature of thermal waters and involves cation (e.g., K–Na, K–Na–Ca and K–Mg) and silica geothermometers. These geothermometers are based on the fundamental assumption of equilibrium between water and mineral at reservoir temperature (Fournier 1977). Reservoir temperature was calculated following the methods: Na–K geothermometer for reservoir temperature > 150 °C (Giggenbach 1988), Na–K–Ca geothermometer for the higher Ca content in geothermal water (Fournier 1977), K–Mg geothermometer for the lower temperatures of 150 °C (Giggenbach 1988). The silica geothermometers are based on solubility of silica phases (e.g., quartz, chalcedony, α -cristobalite and amorphous) and temperature. Quartz geothermometers are

used for the temperature ranging from 150 °C to 225 °C, whereas chalcedony, α -cristobalite or amorphous silica geothermometers are suitable for temperatures below 180 °C (Fournier 1977). The Na–K–Mg ternary diagram proposed by Giggenbach (1988) is an effective tool for determining the equilibrium condition of reservoir fluids and minerals. Several geothermometers are widely applied to estimate reservoir temperature in geothermal systems (Jácome-Paz et al. 2022; Liu et al. 2021), and therefore, they were also discussed in the following section.

Compared to chemical geothermometers, the integrated multicomponent method was more suitable for evaluating the deep reservoir temperature (Spycher et al. 2014; Jácome-Paz et al. 2022; Pérez-Zárate et al. 2022). This approach relies on complete fluid analyses and a solid thermodynamic basis, rather than the solubility of a few minerals or (semi-) empirical correlations (Spycher et al. 2014). Multicomponent geothermometer was performed using the GeoT 2.1 software that involves conducting comprehensive chemical analyses of water samples to compute the saturation indices ($SI = \log(Q/K)$) of reservoir minerals over a temperature range of 25–300 °C (Spycher et al. 2014). The clustering of equilibrium temperature ($SI = 0$) for mineral phase represents the deep reservoir temperature. The statistical functions of SI values, including the median (RMED), mean root square error (RMSE), standard deviation (SDEV), and average (MEAN) of absolute SI values were analyzed using the GeoT 2.1. The bottom temperature was determined as the temperature at which the RMED value approaches zero, indicating equilibrium conditions (Spycher et al. 2016). This calculated bottom temperature was then compared with classical geothermometers: TSF77 (Fournier 1977), TNKVS97 (Verma and Santoyo 1997), and TNKCFT73 (Fournier and Truesdell 1973). The GeoT software's core is the geochemical algorithm that solves mass balance/mass action equations through Newton–Raphson iterations (Spycher et al. 2016). More details on the method are described in Spycher et al. (2016) and Jácome-Paz et al. (2022).

Geochemical modeling

Chemical activity diagrams are effective graphical tools to reconstruct deep reservoir composition and depict mineral-solution equilibria in geothermal system (Bowers et al. 1984; Pérez-Zárate et al. 2022). The activity plots for the $\text{Na}_2\text{O}-\text{Al}_2\text{O}_3-\text{SiO}_2-\text{H}_2\text{O}$, $\text{K}_2\text{O}-\text{Al}_2\text{O}_3-\text{SiO}_2-\text{H}_2\text{O}$, $\text{CaO}-\text{Al}_2\text{O}_3-\text{SiO}_2-\text{H}_2\text{O}$, and $\text{MgO}-\text{Al}_2\text{O}_3-\text{SiO}_2-\text{H}_2\text{O}$ systems were analyzed, assuming the conservation of aluminum (Al) in the solid phase. Aqueous speciation and activity coefficients for thermal spring are computed using the geochemical program PHREEQC with Ilnl thermodynamic database (Parkhurst and Appelo 2013).

Hydrothermal circulation depth calculation

Based on the estimated reservoir temperature, it is possible to quantify the depth of fluid circulation in geothermal areas. The equation (Eq. 2) can be written as follows (Luo et al. 2017):

$$D_c = (T_R - T_A) / \Delta G + H_C, \quad (2)$$

where D_c is the depth of thermal water circulation in m, T_R is the estimated subsurface temperature, the geothermal gradient (ΔG) of 6.5 °C/100 m (Chen et al. 2013), average air temperature (T_A) of 5 °C and constant temperature zone (H_C) at the depth of 20 m.

Results

The location, physical properties, and associated rock types of the collected water samples from the TTYR are listed in Table 1. The chemical and isotopic analytical result for water samples determined in this study with previous data are presented in Tables 2 and 3.

Physico-chemical parameters

The temperature, pH and EC values of thermal springs in the Himalayas range from 13.7 to 87.0 °C, 6.5 to 8.7, and 1873 to 4800 $\mu\text{S}/\text{cm}$, respectively. River water has a temperature of 14.8 °C, a pH of 8.3 and EC of 147 $\mu\text{S}/\text{cm}$. The temperature of groundwater is 7.8 °C with a pH of 8.2 and EC of 203 $\mu\text{S}/\text{cm}$. In the Lhasa block, thermal springs are characterized by temperatures from 37.0 to 75.5 °C, pH from 6.6 to 7.5, and EC from 977 to 6420 $\mu\text{S}/\text{cm}$. The discharge of thermal springs has a wide ranging from 0.50 to 26.0 L/s.

Hydrogeochemistry

Most of the thermal springs along the TTYR display that Na^+ is the dominant cation and HCO_3^- is the prevailing anion. The Na^+ (126–1094 mg/L), K^+ (14.8–133 mg/L), Mg^{2+} (4.17–33.0 mg/L), Ca^{2+} (3.43–316 mg/L) and HCO_3^- (363–2804 mg/L) concentrations of thermal springs in the Himalayas are commonly higher than those of the Lhasa block (7.36–1397 mg/L, 3.69–176 mg/L, 0.02–62.2 mg/L, 0.06–246 mg/L and 151–1621 mg/L). The CO_3^{2-} concentrations are not detected in thermal spring, except for the Labulang thermal spring (362 mg/L, LBL-1). Some thermal springs (BLC-1, MRZ-1, DGSC-1) are characterized by high SO_4^{2-} concentration (514–819 mg/L), whereas samples (SM-1, LBL-1 and MRZ-1) have elevated Cl^- content (674–1000 mg/L). The chemical composition of surface water and groundwater samples is mainly dominated by Ca^{2+} (23.5 mg/L and 29.5 mg/L) and HCO_3^- (80.9 mg/L and 129 mg/L), respectively. The hydrogeochemical facies of thermal springs along the TTYR are mostly Na- HCO_3 and a few thermal springs are mainly Ca- SO_4 and Na-Cl (Fig. 3).

Trace elements concentrations in thermal water from Himalaya range from 1.18 to 5.55 mg/L for Li and 4.72 to 41.30 mg/L for B, whereas thermal waters from the Lhasa block vary from 0.06 to 8.71 mg/L in Li and 0.62 to 61.73 mg/L in B. Rb concentration of thermal springs at the Himalaya and Lhasa block is 0.14–0.79 mg/L and 0.03–1.98 mg/L, respectively, while the Cs concentration range from 0.60 to 1.34 mg/L and 0.05 to 2.55 mg/L, respectively. Thermal spring waters along the TTYR have elevated Sr concentrations of 1.24–3.25 mg/L in the Himalaya and 0.12–6.39 mg/L at the Lhasa block compared to groundwater (0.11 mg/L). Silica concentrations in the Himalayas and Lhasa block are in ranging from 21.5 to 147 mg/L and 21.1 to 130 mg/L, respectively, which are higher than that of groundwater (15.1 mg/L) and surface water (3.91 mg/L).

Stable isotope geochemistry

The stable isotopic compositions of thermal springs along the rift vary from -166 to -135‰ for δD and from -21.4 to -17.0‰ for $\delta^{18}\text{O}$. The δD and $\delta^{18}\text{O}$ values of

Table 1 Field parameters for water samples along the TTYR

No	Name	Water type ^a	Sample ID	Longitude (°E)	Latitude (°N)	Temperature (°C)	EC (µS/cm)	pH	Discharge (L/s)	Rock types at site
<i>Himalayan block</i>										
1	Gongsaba	1	GBSB-1	86.5602	28.4985	13.7	3410	7.26	0.48	ss, ls
2	Canmuda	1	CMD-1	86.4891	28.5994	43.0	2170	6.54	3.0	ss, ls
3	Yundong	1	YD-1	86.7068	28.7924	64.0	1873	6.72	5.7	sl
4	Kajjuacun	1	KJC-1	86.4370	28.9655	18.5	4800	7.24	0.50	sch, lep
5	Nurmigang	1	NIMG-1	86.6104	29.1698	25.4	2350	6.81	2.0	sl, ss
6	Ganglai*	1	GL-1	86.2500	29.1722	87.0	–	7.00	3.0	gn, sl
7	Labulang*	1	LBL-1	86.3850	29.2139	85.0	–	8.65	3.0	sch, sl
8	Semi*	1	SM-1	86.4028	29.2167	86.0	–	–	3.0	sch, sl
9	Gangga	2	GGZ-1	86.6572	28.4851	14.8	147.3	8.28	–	–
10	Gangga	3	GGZ-2	86.5790	28.5836	7.8	203.0	8.22	–	–
<i>Lhasa block</i>										
11	Chazi1	1	CZX-1	86.4774	30.0037	75.5	1912	7.24	26.0	kir, grn, Qal
12	Chazi2	1	CZX-2	86.4769	30.0037	73.4	1922	7.21	–	kir, Qal
13	Chazi3	1	CZX-3	86.4780	29.9994	74.3	1946	7.20	–	kir, Qal
14	Chagang1	1	CG-1	86.4238	30.1557	53.7	1868	7.52	0.50	kir, Qal
15	Chagang2	1	CG-2	86.4261	30.1533	71.7	1433	7.08	–	kir, Qal
16	Daguocun	1	DGSC-1	86.5920	30.4522	37.0	1456	7.16	16.6	tss
17	Banla	1	BLC-1	86.1644	31.0645	58.9	3370	6.76	1.0	Qal
18	Maerzuo	1	MRZ-1	86.6967	31.4722	54.4	6420	6.89	1.5	ss,
19	Dangqiong	1	DQC-1	86.7086	31.6137	48.0	977	6.60	4.1	ss, sl, Qal

"–" not recorded or not determined. a 1-thermal spring; 2-river water; 3-groundwater. * Data from Tong et al., (2000). Abbreviation: ss, sandstone; ls, limestone; sl, slate; sch, schist; lep, leptynite; gn, gneiss; pir, potassic igneous rock; grn, granite; tss, tuff sandstone; Qal, Quaternary alluvium

Table 2 Concentrations of main ions in water samples along the TTYR

No	Name	Sample ID	Na ⁺ (mg/L)	K ⁺ (mg/L)	Mg ²⁺ (mg/L)	Ca ²⁺ (mg/L)	Cl ⁻ (mg/L)	SO ₄ ²⁻ (mg/L)	HCO ₃ ⁻ (mg/L)	SiO ₂ (mg/L)	Charge imbalance	
<i>Himalayan block</i>												
1	Gongsaba	GBSB-1	717	94.8	13.2	57.8	88.1	42.4	2227	42.2	- 3.07%	
2	Gongsaba*	GS-1	728	96.1	13.0	151	99.5	0.10	2258	-	3.71%	
3	Gongsaba*	TB-8	876	133	14.1	186	123	0.70	2343	-	11.30%	
4	Canmuda	CMD-1	356	57.8	28.4	153	22.7	1.06	1499	34.8	3.43%	
5	Canmuda*	TS-1	396	59.9	28.1	148	23.8	1.90	1538	-	4.89%	
6	Canmuda*	TB-1	338	60.4	33.0	121	24.0	1.00	1507	-	- 0.82%	
7	Yundong	YD-1	376	32.6	6.02	54.3	80.0	14.0	1164	58.8	- 3.01%	
8	Kajjucun	KJC-1	1094	64.3	21.3	115	277	43.5	2804	95.3	1.94%	
9	Numigang	NMG-1	126	14.8	34.8	316	52.1	5.93	1604	21.5	- 6.95%	
10	Ganglat**	GL-2	135	19.5	4.57	56.6	88.4	54.1	396	113	- 2.82%	
11	Labulang**	LBL-1	700	87.0	-	-	707	26.5	363	147	-	
12	Semi*	SM-1	700	104	4.17	343	674	65.8	490	116	- 3.07%	
13	Gangga	GGZ-1	2.32	1.30	1.18	23.5	0.28	13.2	80.9	3.91	- 6.94%	
14	Gangga	GGZ-2	5.28	1.63	3.09	29.5	0.33	8.81	129	15.1	- 7.32%	
<i>Lhasa block</i>												
15	Chazi1	CZX-1	446	43.8	0.14	3.73	171	123	817	95.5	8.49%	
16	Chazi2	CZX-2	443	43.8	0.23	4.34	172	123	824	96.0	- 0.14%	
17	Chazi3	CZX-3	440	40.5	0.24	5.17	166	124	850	130.0	- 0.71%	
18	Chagang1	CG-1	384	42.5	-	0.06	260	131	512	88.4	- 1.81%	
19	Chagang2	CG-2	286	23.1	0.02	2.97	197	102	405	112.9	-	
20	Daguocun	DGSC-1	7.36	3.69	62.2	246	1.38	819	151	21.1	- 4.18%	
21	Banla	BLC-1	851	45.8	5.72	35.0	155	514	1610	70.3	- 6.32%	
22	Maerzuo	MRZ-1	1397	176	8.31	41.9	1000	786	1621	92.1	- 2.40%	
23	Dangqiong	DQC-1	93.6	12.4	21.7	87.1	9.51	108	518	42.6	- 1.35%	

The CO₃²⁻ concentration of the LBL-1 sample is 362 mg/L. "-" below detection limits, or not analyzed. * data from Newell et al. (2008); ** data from Tong et al. (2000)

Table 3 Concentrations of trace elements and O–H–Sr isotopic compositions in water samples along the TTYR

No	Name	Sample ID	Sr (mg/L)	Li (mg/L)	B (mg/L)	Rb (mg/L)	Cs (mg/L)	$\delta^{18}\text{O}$ (‰)	δD (‰)	$^{87}\text{Sr}/^{86}\text{Sr}$
Himalayan block										
1	Gongsaba	GBSB-1	2.16	4.46	15.48	0.73	1.16	– 20.3	– 163	0.7293
2	Canmuda	CMD-1	1.43	1.85	7.34	0.30	0.60	– 20.6	– 162	0.7317
3	Yundong	YD-1	1.24	3.10	22.73	0.35	1.34	– 21.3	– 170	0.7158
4	Kajucun	KJC-1	2.68	5.55	41.30	0.79	0.61	– 19.4	– 159	0.7166
5	Numigang	NIMG-1	3.25	1.18	4.72	0.14	0.86	– 21.3	– 166	0.7111
6	Gangga	GGZ-1	–	–	–	–	–	– 18.2	– 135	–
7	Gangga	GGZ-2	0.11	0.04	0.29	0.003	<0.001	– 21.2	– 160	0.7189
Lhasa block										
8	Chazkiang1	CZX-1	0.64	2.32	39.96	0.64	1.36	– 20.2	– 161	0.7143
9	Chazkiang2	CZX-2	0.66	2.37	40.63	0.64	1.37	– 20.2	– 161	0.7142
10	Chazkiang3	CZX-3	0.65	2.28	37.93	0.58	1.26	– 20.3	– 161	0.7141
11	Chagang1	CG-1	0.18	4.72	61.73	0.74	2.55	– 17.5	– 151	0.7180
12	Chagang2	CG-2	0.12	4.17	49.63	0.35	1.54	– 18.4	– 152	0.7168
13	Daguocun	DGSC-1	6.39	0.06	0.62	0.03	0.05	– 19.7	– 144	0.7106
14	Banla	BLC-1	1.91	1.28	3.67	0.29	0.68	– 18.4	– 156	0.7103
15	Dangqiong	DQC-1	0.83	0.76	2.25	0.09	0.29	– 18.5	– 145	0.7165
16	Maerzuo	MRZ-1	0.92	8.71	34.73	1.98	1.39	– 17.0	– 135	0.7135

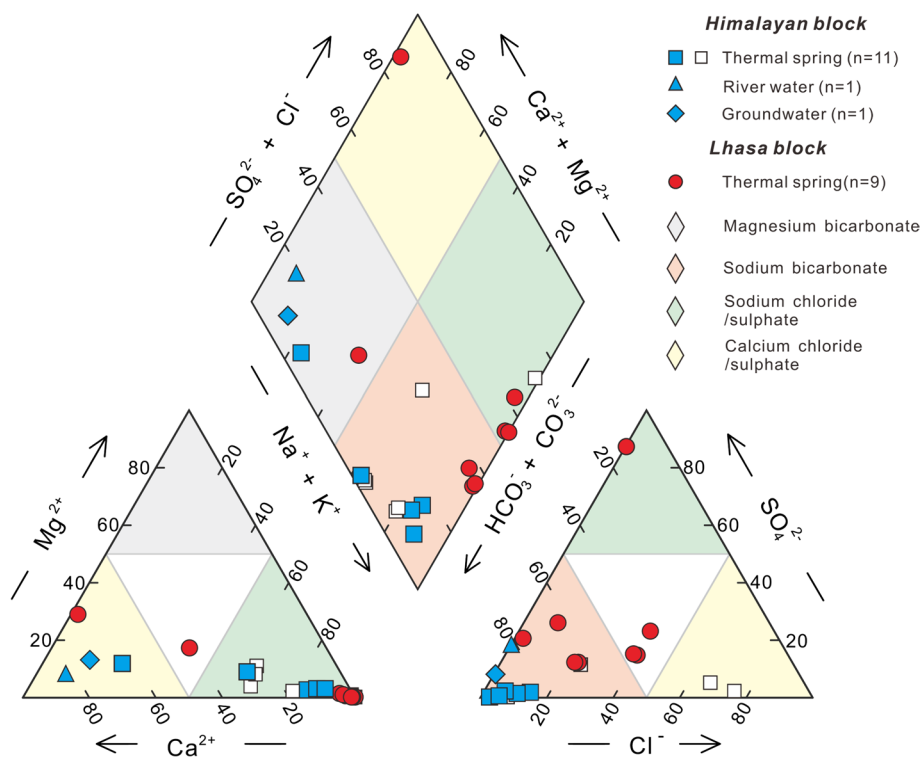


Fig. 3 Piper diagram showing the major ion content of thermal waters along the TTYR. Filled and open symbols represent this study and literature data (Newell et al. 2008; Tong et al. 2000), respectively

surface water and groundwater range from -164 to -135‰ and -21.9 to -17.6‰ , respectively. Thermal springs from the Himalayas yield a relatively wide range in $^{87}\text{Sr}/^{86}\text{Sr}$ values (0.7111 to 0.7317) compared to thermal springs in the Lhasa block (0.7103 to 0.7180). The $^{87}\text{Sr}/^{86}\text{Sr}$ ratio of shallow groundwater is 0.71887.

Discussion

Origin and recharge of hydrothermal water

δD and $\delta^{18}\text{O}$ values from thermal springs as well as surface and well water are plotted in Fig. 4. All water samples lie on or close to both the global meteoric water line (GMWL) and the local meteoric water line (LMWL), indicating a dominantly meteoric origin. A few thermal spring samples display a small $\delta^{18}\text{O}$ shift from the meteoric water line compared to surface water and groundwater. This shift was known as the geothermal shift in many previous studies, attributed to water–rock interaction at high-temperature geothermal systems and/or evaporative process (Luo et al. 2017). It is possibly caused by ^{18}O isotopic exchange between thermal fluid and oxygen-bearing minerals within the reservoir rock depending on reservoir temperature, mineralogy, the permeability of the rocks, and the time of the water–rock reaction (Liu et al. 2022 and references therein). In addition, a similar trend was observed in thermal springs from the Yadong-Gulu rift (Zhou et al. 2023) and Cuona rift (Wang et al. 2020) in the HTO, which may be attributed to the mixing of snowmelt water with some contribution from magmatic water in the geothermal system.

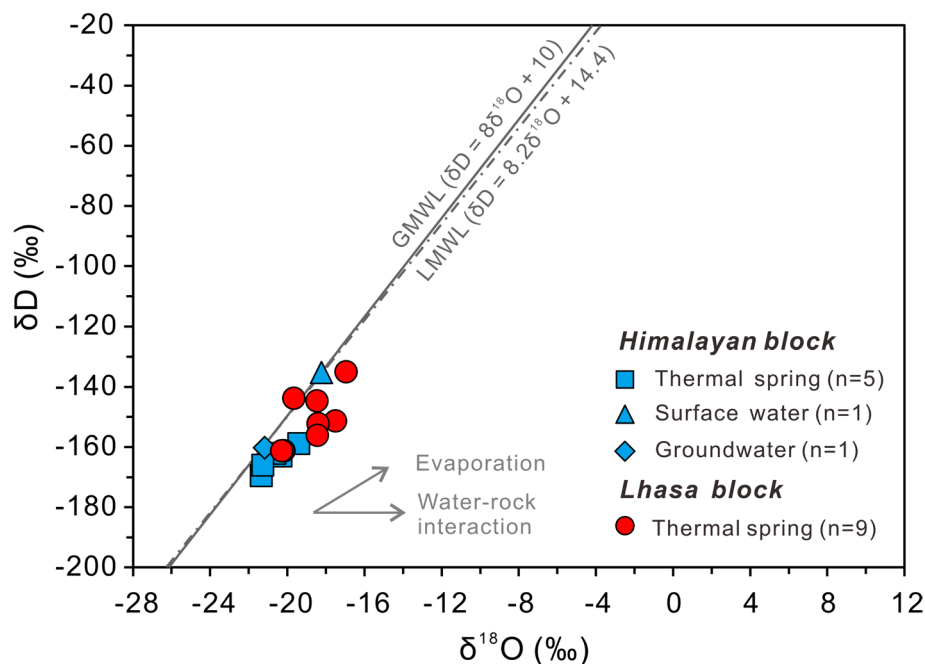


Fig. 4 Plot of $\delta^{18}\text{O}$ versus δD values of water samples from the TTYR along the global meteoric water line (GMWL, Craig 1961) and the local meteoric water line (LMWL, Tan et al. 2014)

Thus, the calculated recharge elevation for geothermal water was estimated to be 5400–5758 m.a.s.l. in the Himalayas and 4617–5844 m.a.s.l. in the Lhasa block (see Table S1 in supplementary material). Numerous mountains around thermal springs along the TTYR have an average elevation of 5500–6000 m. The calculated recharge elevation of thermal springs is very close to that of the peaks of these mountains, suggesting that thermal springs are derived from meteoric water around the mountains.

Water–rock interactions of hydrothermal circulating

The chemical composition of thermal water is generally affected by different chemical reactions of precipitation water such as the dissolution of carbonate, silicate, halite, and gypsum, precipitation, and ion exchange processes during the hydrothermal circulation processes (Negri et al. 2018). Ca^{2+} and Mg^{2+} are commonly derived from the dissolution of carbonate and dolomite whereas Na^{+} and K^{+} are originated from silicate minerals (e.g., pyroxene, albite, and K-feldspar) in hydrothermal systems (Eqs. 1–6). Carbonate and dolomite dissolution are characterized by a molar ratio of 1:2 for $(\text{Ca}^{2+} + \text{Mg}^{2+})/\text{HCO}_3^-$. In the $(\text{Ca} + \text{Mg})$ vs. HCO_3^- diagram (Fig. 5a), most thermal waters plot below the theoretical line of carbonate and dolomite dissolution, suggesting the existence of additional sources of HCO_3^- . HCO_3^- is easily converted by carbonic acid that is originated from the dissolution of ascending CO_2 from crust and mantle degassing along the fault zone into shallow groundwaters in these geothermal areas (Eqs. 3 and 4). The CO_2 -dominated bubbling gases from thermal springs along the TTYR are derived from metamorphic decarbonation in the crust (> 80%) with the lower mantle carbon (< 20%) (Klemperer et al. 2022; Liu et al. 2024). Except for sample LBL-1, all thermal waters have slightly acidic to near neutral pH (from 6.5 to 7.5).

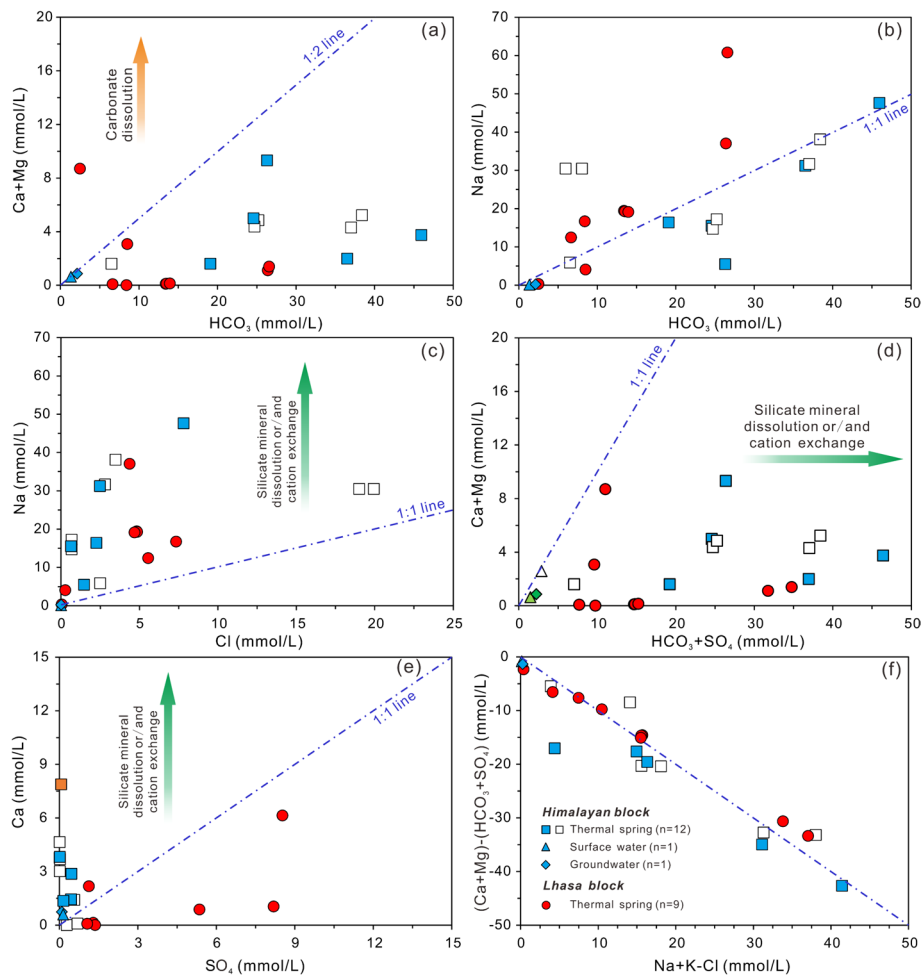
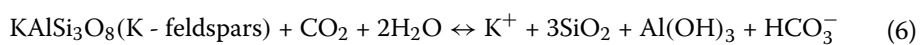
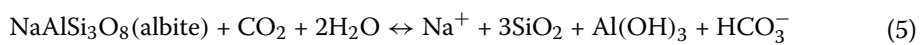
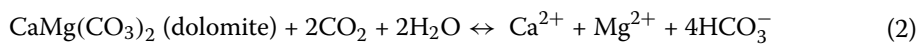
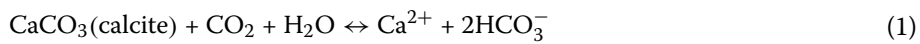
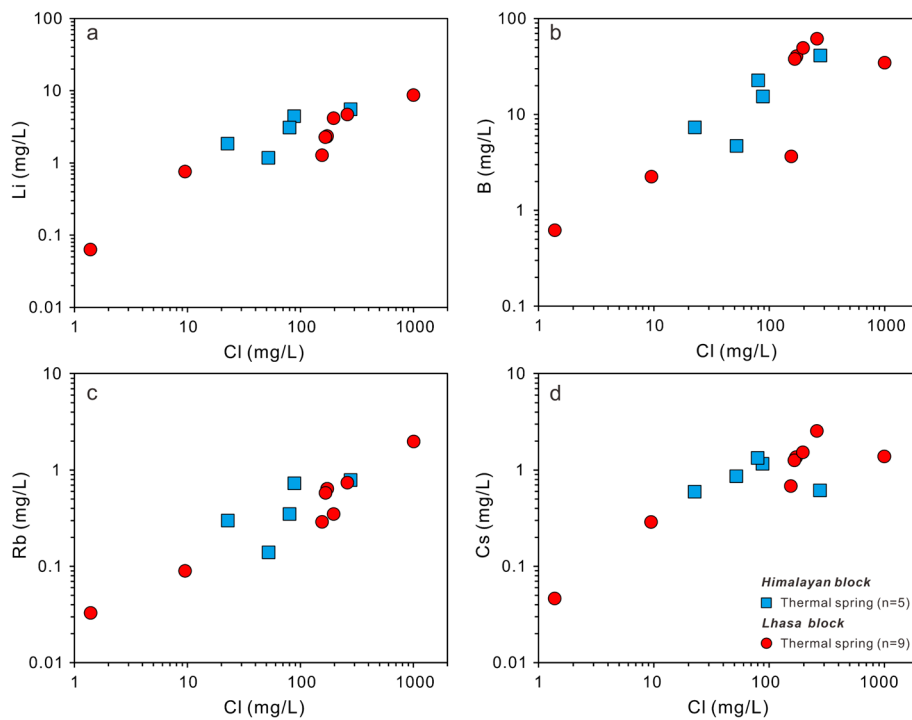
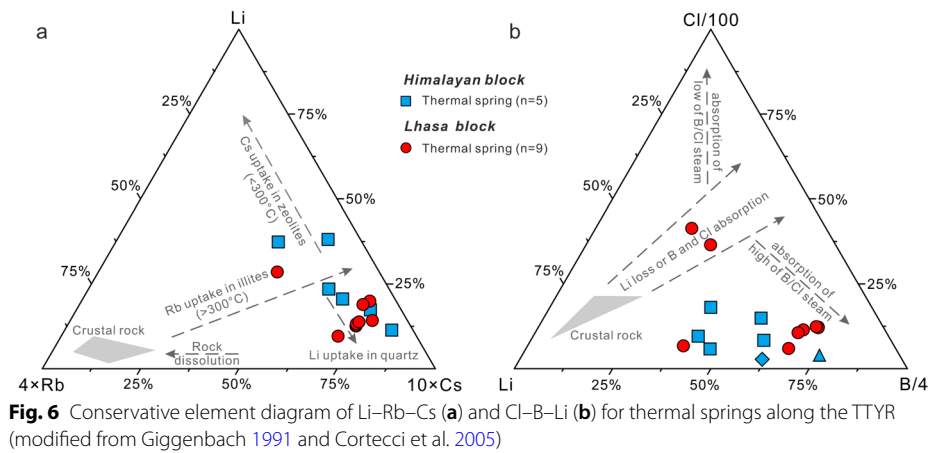


Fig. 5 Composition diagram for water samples along the TTYR. Filled and open symbols represent this study and literature data (Newell et al. 2008; Tong et al. 2000), respectively





Most thermal waters are Na-HCO₃ type, which is commonly associated with the weathering of silicate in carbonic acid aquifers. The enrichment of HCO₃⁻ in thermal springs from the Himalayas may also be attributed to the weathering of silicate minerals in the presence of CO₂ in the aquifers (e.g., albite and K-feldspars; Eqs. 5 and 6; Fig. 5b). Higher SiO₂ content and Na/Cl ratios > 1 relative to surface water further support that the chemical composition of thermal waters is affected by the weathering of silicate (Fig. 5c), which is supported by the plot of HCO₃⁻ + SO₄²⁻ vs. Ca + Mg (Fig. 5d). The dissolution of carbonates and sulfate minerals by circulating fluids would result in Ca²⁺, Mg²⁺, HCO₃⁻ and SO₄²⁻ in equimolar concentration. The plots of all thermal

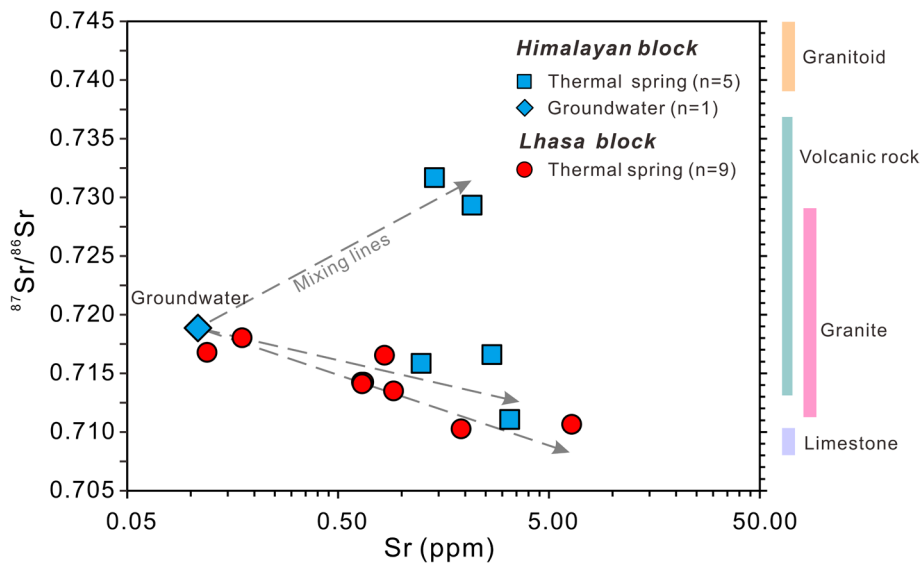


Fig. 8 Plot of $^{87}\text{Sr}/^{86}\text{Sr}$ vs. Sr content showing ternary mixing model for thermal springs along the TTYR. The $^{87}\text{Sr}/^{86}\text{Sr}$ ratios of limestone, Cenozoic granitoid, Gangdese granites and volcanic rocks are from Négrel and Roy, (1998), Fan et al. (2021) and Mao et al. (2012), Wang et al., (2015) and Guo et al. 2013, respectively

waters are well below the 1:1 line in the $(\text{Ca}^{2+} + \text{Mg}^{2+})$ versus $(\text{HCO}_3^- + \text{SO}_4^{2-})$ diagram. In addition, the excess $\text{HCO}_3 + \text{SO}_4$ may also originate from deeper sources (e.g., deep fluids) in addition to the dissolution of sulfide minerals at the shallow

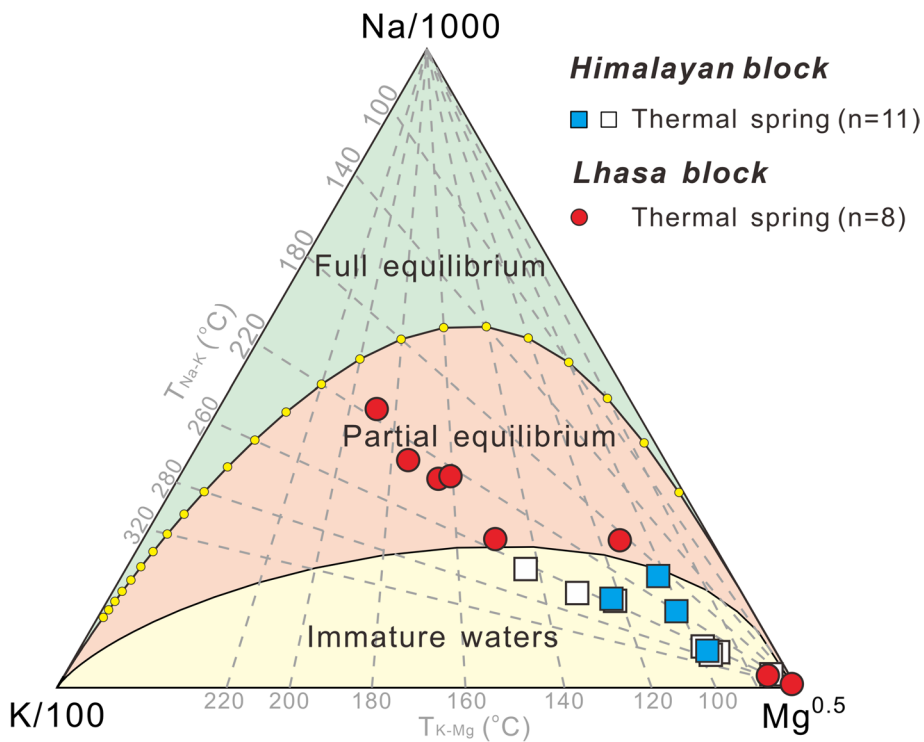


Fig. 9 The Na–K–Mg ternary diagram (after Giggenbach 1988) for thermal springs along the TTYR

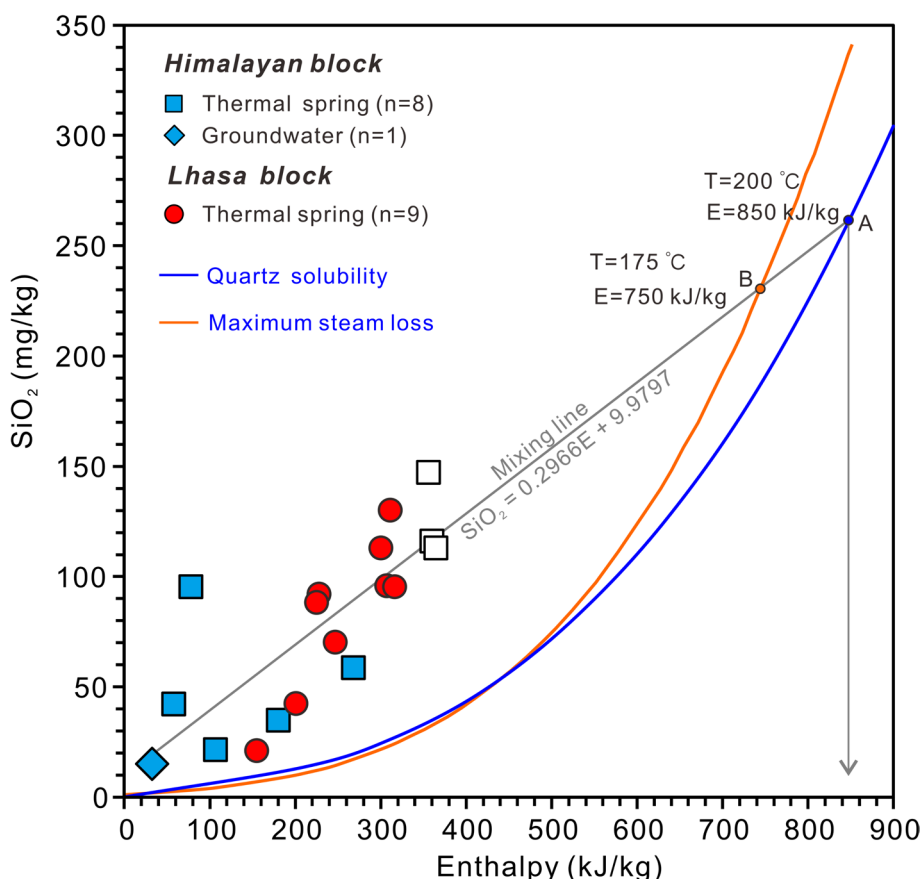


Fig. 10 Silica enthalpy mixing model (after Truesdell and Fournier 1977) for thermal waters along the TTYR. The reservoir temperature can be estimated from the intersection of the mixing line (adding cold water to hot water sample) with the quartz solubility curve, which assuming no steam or heat steam loss occur before mixing. The calculated bottom temperature for thermal spring from the TTYR is 175 °C and a maximum temperature of 200 °C

aquifer depths or evaporite mineral such as gypsum (Bucher and Stober 2010; Liu et al. 2022). In the Ca vs. SO₄ diagram (Fig. 5e), Ca²⁺ concentrations for most thermal waters in the Himalayas are higher than those of the Lhasa block, suggesting that carbonate dissolution can explain Ca²⁺ excess relative to SO₄²⁻. This result is consistent with the observation of carbonate rocks in the Himalayas. Thermal springs in the Himalayas have a low SO₄²⁻ content indicating sulfate reduction. In contrast, thermal waters with the SO₄²⁻ enrichment in the Lhasa block are probably attributed to the oxidation of H₂S in the geothermal system (Abdelali et al. 2020), which is supported by the significant H₂S smell and sulfide deposits at the surface around Chazi and Banla thermal springs. On the other hand, high SO₄²⁻ contents in thermal water are also related to leaching from sulfate-bearing host rock of Cenozoic volcanic rocks along the TTYR in the Lhasa block (Li et al. 2019). In addition, most thermal waters are close to the 1:1 line in the (Ca + Mg)–(SO₄ + HCO₃) vs. (Na + K)–Cl diagram and are characterized by (Na⁺ + K⁺) enrichment and (Ca²⁺ + Mg²⁺) depletion, indicating that ion exchange reaction is an important process (Fig. 5f). The reaction for cation exchange are (Fisher and Mullican 1997):

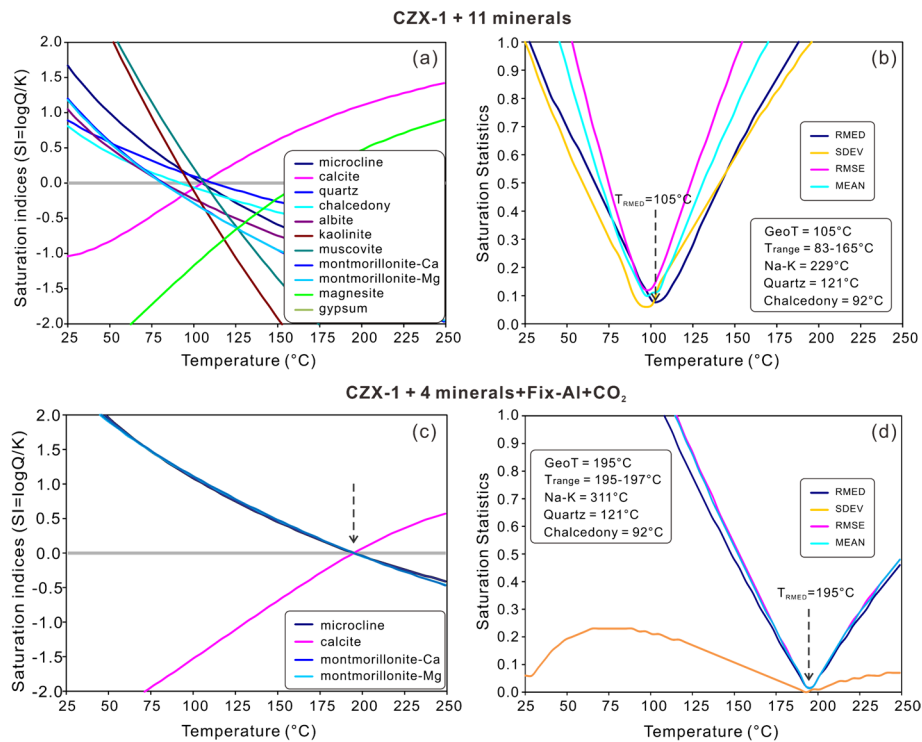
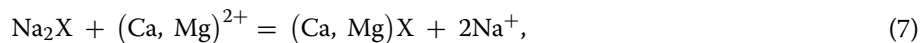


Fig. 11 Saturation index (SI = log Q/K) and statistical parameters computed with GeoT for sample CZX-1 from Chazi thermal springs. **a** The 11 input minerals; **b** statistical analyses of SI for 11 minerals; **c** the selected 4 input minerals after applying the Fix-Al method, CO₂ degassing correction and dilution factor; **d** statistical analyses of saturation indices for 4 minerals. RMED, RMSE, SDEV and MEAN represent median, mean root square error, standard deviation and average of absolute SI values. The saturation indices of these minerals are computed over a range from 25 °C to 250 °C. The estimated temperature (GeoT) is indicated by the arrow with the lowest SI values. The temperature range (Trange) is determined by the temperatures at which the SI of each mineral equals 0. Temperature estimates from chemical geothermometers are also shown



where X represents an ion exchange site occupied by two monovalent or divalent cation.

Conservative elements such as Li, Rb, Cs, and B in thermal water are useful for providing formation processes of hydrothermal fluid due to their ratios being unaffected by the dilution or boiling processes (Cortecchi et al. 2005; Giggenbach and Soto 1992; Munoz-Saez et al. 2020; Zhou et al. 2023). Li uptakes in secondary quartz with abundant fluid inclusions (Drüppel et al. 2020) and chlorite may be derived from rock dissolution (Giggenbach and Soto 1992). B is probably derived from the dissolution of feldspar in granitic reservoir rocks at depth (Stober et al. 2016) and absorption of B-rich vapors in water. Cs is incorporated into zeolites below about 250 °C, whereas Rb is taken up by secondary clays and illites at quite high temperatures (> 300 °C) (Öztekın Okan et al. 2018; Shakeri et al. 2008). These rare alkalis were characterized by incompatible behavior and acquired by the geothermal waters at the early stages of fluid–rock interaction along the flow path (Giggenbach and Soto 1992). These waters in the geothermal system remain comparatively stable and not generating secondary minerals (Goguel 1983; Kaasalainen and Stefánsson 2012; Zhou et al. 2023). All thermal waters are far from the average composition of crustal rock and fall close to

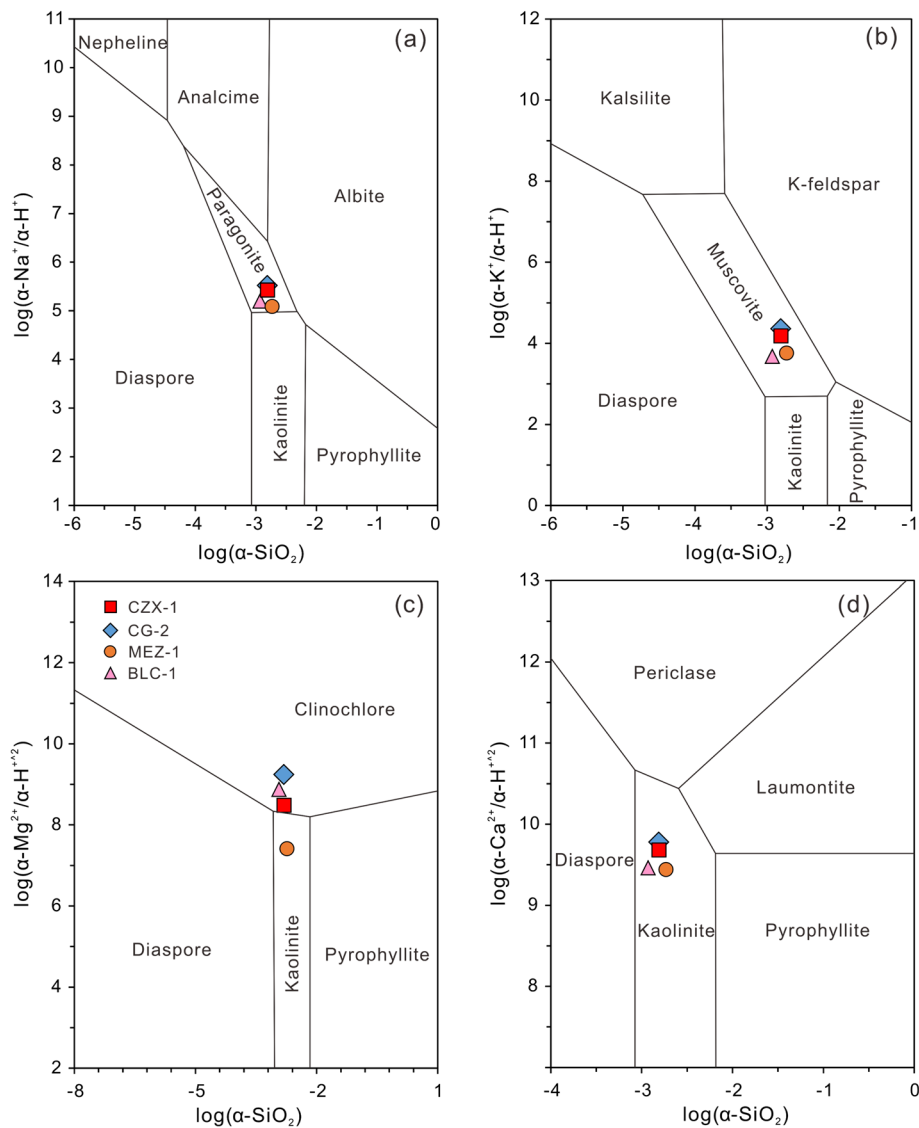


Fig. 12 Activity plots for the systems: **a** $\text{Na}_2\text{O}-\text{Al}_2\text{O}_3-\text{SiO}_2-\text{H}_2\text{O}$, **b** $\text{K}_2\text{O}-\text{Al}_2\text{O}_3-\text{SiO}_2-\text{H}_2\text{O}$, **c** $\text{MgO}-\text{Al}_2\text{O}_3-\text{SiO}_2-\text{H}_2\text{O}$, and **d** $\text{CaO}-\text{Al}_2\text{O}_3-\text{SiO}_2-\text{H}_2\text{O}$ at the mean temperature of 171 °C

the Cs apex in the Li–Rb–Cs diagram, showing a significant depletion in Rb content (Fig. 6a). The depletions are related to the occurrence of the secondary processes during geothermal fluid ascent.

The relative proportions of Cl, Li and B in thermal water are shown in the Cl–Li–B ternary diagram to delineate the formation processes of geothermal fluids. Most thermal waters have formed through the absorption of B-rich or lower Cl vapors. The B/Cl ratios have been used to identify the type of reservoir rocks traversed by geothermal fluids in active hydrothermal systems (Reyes and Trompeter 2012). Thermal waters along the TTYR with B/Cl ratios of 0.02 to 0.45 are higher than that of rhyolite water (0.01 to 0.02) and andesite water (0.02 to 0.07) in the Taupo Volcanic Zone, New Zealand (Reyes and Trompeter 2012). Most of the thermal springs are plotted near to the B apex with a high B/Cl weight ratio (Fig. 6b). Elevated B concentrations

in some thermal spring indicate hydrothermal fluid flowing through igneous rocks (e.g., tourmaline, biotite and amphiboles) along the fault zones (Pantić et al. 2015). This result is supported by the wide distribution of Meso-Cenozoic granite intrusions and volcanic rocks along the TTYR. Relationships between Li, Rb, Cs, and B in thermal spring waters along the TTYR compared to the rock ratios of basalt and rhyolite (see Fig. S1 in supplementary material) suggest the absorption of the higher B from magmatic degassing, the preferential release of B through the leaching of rock, and/or the uptake of Li, Cs, and Rb in secondary minerals such as fluid inclusions in quartz, illite and zeolite, as observed in other geothermal waters (Kaasalainen and Stefánsson 2012; Shaw and Sturchio 1992). Trace element contents (e.g., Li, B, Rb and Cs) show a different positive correlation with Cl, suggesting a different reservoir and hydrogeochemical processes (Fig. 7). The relative content of the conservative elements (e.g. Cl, B and Li) observed in thermal waters may be related to a long residence time of geothermal fluids and to enhance water–rock reactions at the high temperatures (Drüppel et al. 2020).

Strontium isotope constraints on hydrogeological reservoirs

Strontium in thermal water is dissolved from the surrounding rocks and derived from water–rock isotopic exchange occurring at an equilibrium state (Notsu et al. 1991). Sr isotopic compositions of hydrothermal fluid serve as an indicator for understanding the path of circulating fluid and reflecting those of the host rock (Isaji et al. 2021; Tardani et al. 2021). Generally, carbonate and evaporate rocks have high Sr content and low $^{87}\text{Sr}/^{86}\text{Sr}$ values, whereas silicate rocks display low Sr content and high $^{87}\text{Sr}/^{86}\text{Sr}$ (Palmer and Edmond 1992). The $^{87}\text{Sr}/^{86}\text{Sr}$ ratios vs Sr content diagram indicates the different end-members of Sr source for thermal springs along the TTYR (Fig. 8). The $^{87}\text{Sr}/^{86}\text{Sr}$ ratios of thermal springs in Himalaya have a wide range of 0.71106 to 0.73169 and are between that of Cenozoic granitoid (mean $^{87}\text{Sr}/^{86}\text{Sr}=0.7413\pm 0.0029$; Fan et al. 2021; Mao et al. 2012) with limestone ($^{87}\text{Sr}/^{86}\text{Sr}=0.7068\text{--}0.7094$; Négre and Roy 1998) and the sampled groundwater ($^{87}\text{Sr}/^{86}\text{Sr}=0.71887$). These data patterns are attributed to several processes including shallow groundwater mixing with the geothermal fluid hosted in granitoid and carbonate rocks. The highest $^{87}\text{Sr}/^{86}\text{Sr}$ ratios of two springs (Gongbasaba

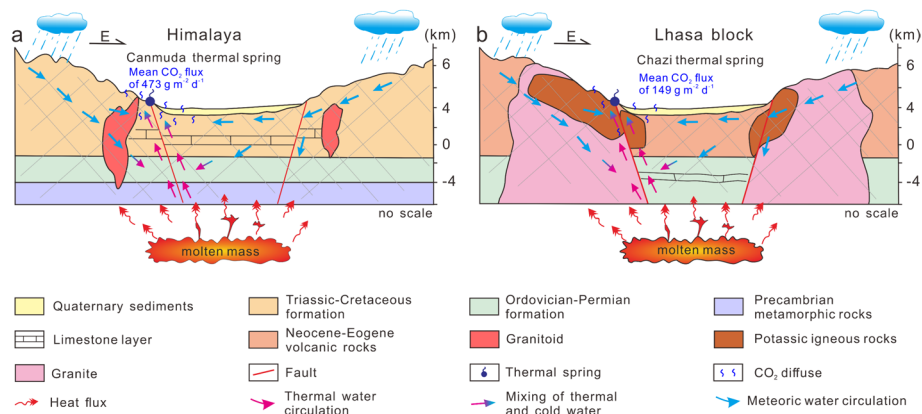


Fig. 13 Conceptual model of the geothermal systems in the Himalayas (a) and Lhasa block (b). The mean soil CO₂ diffuse fluxes of Canmuda and Chazi thermal spring are from Liu et al. (2024)

spring and Canmuda spring) in the Himalayas indicate long fluid flow through deep granitic rocks or Precambrian basement (Fig. 8). This is supported by the presence of inter-bedded carbonate sediments, Meso-Cenozoic granitoid and minor metamorphic rocks in the Himalayas (Newell et al. 2008). Host rocks of thermal springs in the Lhasa block are dominated by Gangdese granites and Linzizong volcanic rocks. The $^{87}\text{Sr}/^{86}\text{Sr}$ ratios of the hot springs in the Lhasa block are slightly lower than that of host Gangdese granites (mean $^{87}\text{Sr}/^{86}\text{Sr} = 0.7201 \pm 0.0084$; Wang et al. 2015) and volcanic rocks (mean $^{87}\text{Sr}/^{86}\text{Sr} = 0.7226 \pm 0.0062$; Guo et al. 2013) indicating a mixture of groundwater and fluid interaction with granites, volcanic rocks. Two samples in the Lhasa block are close to groundwater indicating the amount of shallow groundwater mixed into the hydrothermal system.

Reservoir temperature and circulation depth

The reservoir temperatures estimated for thermal springs along the TTYR are given in Table S2 within supplementary material. With the exception of Daguocun thermal spring (DGSC-1), the Na/K geothermometer yields a wide temperature ranging from 166 to 297 °C, which is higher than those of K/Mg (46 to 158 °C) and K/Na/Ca (114 to 198 °C) geothermometers. The lower reservoir temperatures calculated using the K–Mg geothermometer are associated to mixing with shallow groundwater and/or result of thermal water disequilibrium. Some thermal spring samples in Lhasa block are plotted along the ~220 °C Na–K isotherm and partially equilibrated waters field, indicating equilibrium of thermal fluid with the feldspars in the reservoir rock (Fig. 9). However, the distribution of thermal water samples is dispersed along the Mg–K vector due to incomplete equilibrium with a mineral assemblage that controls Mg (Stober and Bucher, 2010; Stober et al. 2016). Thermal waters located in the area of immature water suggest mixing with shallow nonthermal groundwater before being discharged in springs and/or have limited interaction with host rocks in the reservoir. The SiO_2 geothermometer may provide a minimum reservoir temperature for thermal springs in open systems (Stober et al. 2016). Calculated reservoir temperature for the silica geothermometers relies on the solubility of silica polymorphs such as quartz, chalcedony, cristobalite, amorphous silica, etc. The calculated temperatures by α -cristobalite and amorphous silica geothermometers for some thermal springs are below the measured surface temperature (e.g., Canmuda, Yundong, Numigang, Daguocun and Dangqiong spring) or negative, suggesting that these geothermometers are possibly inaccurate (see Table S2 in supplementary material). The quartz geothermometer estimates reservoir temperatures varying from 65 to 160 °C, which is only a few degrees above that of the chalcedony geothermometers (37 to 132 °C). Note that thermal springs have experienced less fluid–rock reaction and mixing of shallow groundwater during fluid ascent and cooling by precipitation of silica phases along the flow paths. Therefore, the temperature calculated by the quartz geothermometer probably represents the lowest values.

The silica-enthalpy mixing model published by Truesdell and Fournier (1977) have been extensively used to determine bottom temperature of a hot-water component mixed with cold water. This diagram assumes that no steam loss and maximum steam loss occurs before mixing. We choose GGZ-1 samples ($T = 7.8$ °C and $\text{SiO}_2 = 15.1$ mg/L) as groundwater end-member. The intersection of the mixing line of cold water to

thermal water with the quartz solubility maximum and steam loss curve calculate the bottom temperature of 175 °C and 200 °C for thermal springs along the TTYR (Fig. 10). The deep reservoir temperature is about 200 °C equal to 850 kJ/kg.

Chemical geothermometers can be influenced by various processes, such as mixing with cold waters, precipitation, and boiling, during their migration to the surface. These processes can obscure the deep geochemical signature. The multicomponent geothermometry is considered to be a reliable and realistic method to estimate deep reservoir temperatures (Spyche et al. 2016; Jácome-Paz et al. 2022; Pérez-Zárate et al. 2022). In a first step a large list of 11 minerals assemblage including microcline, calcite, Ca-montmorillonite, Mg-montmorillonite, albite, quartz, kaolinite, chalcedony, muscovite, magnesite and gypsum, are used. Sample CZX-1 collected from main outlet of thermal springs have a highest temperature (75.5 °C) and low pH (7.24), indicating minor CO₂ loss and the close to reservoir composition. The chemical composition from the CZX-1 together with 11 minerals are calculated in Geo T. The saturation index curves of the 11 mineral phases are computed over a range from 25 to 250 °C (Fig. 11a). The temperature estimated from the lowest RMED (TRMED) value is 105 °C (Fig. 11b). However, the estimated result remains uncertain due to a broad range of temperatures (83 to 165 °C) defined by the equilibrium line crossing (SI = 0). Obviously, chemical equilibrium between water and a mass of minerals in the reservoir is impossible in geothermal system. The multicomponent method utilizes an elimination algorithm to automatically refine the selection of minerals. The selected four “best-clustering” minerals include: calcite, microcline, Ca-montmorillonite and Mg-montmorillonite. The estimated equilibrium temperature (from the minimum RMED value) is 195 °C (Fig. 11c and d). The SI curves for four mineral phases display a tight clustering around zero defined by a narrow T_{range} (195–197 °C), following the application of the Fix AI method, CO₂ degassing correction and dilution factor (See Pang and Reed 1998 for more details).

Subsequently, we employed the same methodology to water sample (i.e., CG-2, BLC-1 and MRZ-1) from other thermal springs. The temperature estimated (TRMED) values range from 115 °C to 195 °C with a mean of 171 °C (see Fig. S2 and Table S3 in supplementary material). Notably, the saturation index (SI) curves consistently indicated that these four minerals always reached equilibrium at the estimated temperature. This result estimated by multicomponent geothermometer is overlapped by the range in chemical geothermometers (Na–K and Na–K–Ca), indicating that the thermal fluid interacts with calcite, microcline, Ca-montmorillonite and Mg-montmorillonite at reservoir temperatures between 115 °C with 195 °C. In addition, we use activity diagrams to evaluate mineral–solution equilibrium in the reservoir. The average bottom temperature of 171 °C in this study is chosen as reference temperature for the construction of the activity plots. In Fig. 12a and b, thermal water samples are situated in the field of paragonite (muscovite) or close to the stability line of kaolinite indicating that the activity of dissolved Na⁺ and K⁺ is related to one of these solid phases. This agrees with the results obtained by Na/K geothermometers, indicating these minerals are close to the stable phase in equilibrium with the thermal waters. In Fig. 12c and d, samples are also plot in the kaolinite stability field or near kaolinite–clinochlore coexistence line. The dissolved Ca²⁺ and Mg²⁺ are controlled by kaolinite and clinochlore. These minerals are saturated at reservoir temperatures. Based on the

estimated reservoir temperature with the multicomponent geothermometry, these thermal springs along the TTYR calculate the circulation depths from 1712 to 2943 m (see Table S3 in supplementary material).

Knowing reservoir temperature and the discharge of thermal springs along the TTYR, it is possible to estimate convective heat discharge from the geothermal system (Sorey and Lewis 1976). The calculated heat fluxes range from 3.96×10^5 J/s at Banla thermal spring to 1.78×10^7 J/s at Chazi thermal spring (see Table S3 in supplementary material). The convective heat flow from thermal springs along the TTYR is comparable with those of the Lucane (7.75×10^6 to 2.00×10^7 J/s) and Sambiasse (5.40×10^6 J/s) geothermal system in southern Apennines (Italy, Apollaro et al. 2020 and references therein).

Conceptual model

Since the Cenozoic, the Tibetan Plateau has undergone intense tectonic deformation, forming a series of north–south trending extensional rifts composed of many large-scale normal faults. Hot springs are spatially controlled by extensional faults along the TTYR. These large faults facilitate the transport of deep-seated heat energy and geothermal fluids to the surface. Based on the geological structures of the TTYR and chemical and isotopic compositions of hydrothermal water, we propose a conceptual model for the formation of hot springs in the Himalayas and Lhasa block (Fig. 13). The thermal waters are mainly recharged by meteoric waters from the adjacent mountainous areas with elevations above 6000 m. Based on chemical and multicomponent geothermometers, the best-estimated reservoir temperatures for thermal spring at partial equilibrium are 115–195 °C. The estimated convection heat discharge of hydrothermal systems along the TTYR range from 3.96×10^5 J/s to 1.78×10^7 J/s. The infiltration of meteoric water along the fault zone or rock fractures can reach depths of about 1700–2900 m, and attain high temperature via heating by geothermal gradient or conductive heating by deep-derived magmatic fluids. Geophysical investigations in the Himalayas and southern Tibet show a low-resistivity layer and/or seismic bright spots at a depth of 20–25 km, which was interpreted as a partially molten layer (Nábělek et al. 2009; Unsworth et al. 2005). Thus, the partial melt can be considered as the potential heat source for the thermal springs. The high concentrations of Na^+ and HCO_3^- in thermal waters are associated with the dissolution of silicate and carbonate rocks during water–rock interaction and the contribution of deep CO_2 . The geochemical composition of thermal springs in the Himalayas is controlled by interaction of water with granitoid and carbonate rocks, while those of thermal spring in the Lhasa block may be due to mixing groundwater with interaction between hydrothermal fluid and granite and volcanic rocks. The geothermal fluids ascend through fault and/or fracture systems toward the surface, mix with groundwater at the shallow depth and experience different degrees of water–rock interaction at the different geologic and tectonic units.

Conclusions

A series of hot springs associated with the faults along the TTYR in the HTO are analyzed for their chemical and isotopic compositions. Some conclusions can be reached:

1. The hydrothermal waters are dominantly meteoric origin and a small contribution of magmatic component. The meteoric water recharge likely occurs from elevations of 4617 to 5844 m.a.s.l.
2. The hydrothermal waters are chemically Na-HCO₃ type with few Na-SO₄ and Na-Cl types. The water chemical compositions are mainly controlled by meteoric water interacting with granitoid, granite and carbonate during infiltration and circulation of meteoric water. Other processes such as ion exchange and mixing with cold groundwater are also contributed to the variation of chemical composition.
3. The best-estimated reservoir temperatures of hydrothermal waters are from 115 to 195 °C, corresponding to the depth of fluid circulation from 1700 to 2900 m along the fault systems. As such, the heat flow of the geothermal systems is estimated from 3.96×10^5 to 1.78×10^7 J/s, which is comparable to the low-enthalpy geothermal system in southern Italy. These demonstrate that extensional fault systems of the TTYR are preferential conduits to transfer deep geothermal fluid and heat to the surface.

Supplementary Information

The online version contains supplementary material available at <https://doi.org/10.1186/s40517-024-00311-8>.

Additional file 1: Fig. S1. Relationships between Li, Rb and Cs vs. B for thermal springs along the TTYR. The dashed line and chain-dotted line represent the median rock ratios of basalt and rhyolite as defined by Kaasalainen and Stefánsson, respectively. Symbols are the same as in Fig. 6. **Fig. S2.** Saturation index and statistical parameters computed with GeoT for CG-2, BL-1 and MRZ-1 thermal springs. Results are presented by applying the Fix-AI method, CO₂ degassing correction, dilution factor, and the selected four selected minerals. **Table S1** The calculated recharge elevations of thermal springs along the TTYR. **Table S2** Estimated reservoir temperatures of thermal water along the TTYR. **Table S3** Deep reservoir temperature calculated by the multicomponent method and circulation depth and heat fluxes for considered thermal springs along the TTYR.

Acknowledgements

Lufeng Guan, Shuncheng Zhang and Hanyu Wang are thanked for their assistance and support in the field. We are grateful to Zhenping Cao, Yufei Jin, Xiaobo Li, Xunan Meng and Lixin Zhang for their help in laboratory analysis.

Author contributions

WL, MZ, and LC conducted field campaign and collected the samples. WL and YL analyzed samples and compiled geochemical data. WL performed data visualization and all authors interpreted the data to establish a conceptual model. WL wrote the draft manuscript and SX, MZ, and YS are major contributors to review and edit the manuscript. All authors have read and approved the final manuscript.

Funding

This study was supported by National Natural Science Foundation of China (NSFC) (41930642) and National Key Research and Development Project (2020YFA0607700). MZ acknowledges an NSFC Grant 42072327.

Availability of data and materials

All data supporting the findings in this study are provided in Tables 1–3 and the Supplementary materials.

Declarations

Competing interests

The authors declare that they have no known competing financial interests or personal relationships that could have appeared to influence the work reported in this paper.

Received: 1 February 2024 Accepted: 20 August 2024

Published online: 03 September 2024

References

- Abdelali A, Nezli IE, Kechiched R, Attalah S, Benhamida SA, Pang Z. Geothermometry and geochemistry of groundwater in the Continental Intercalaire aquifer, southeastern Algeria: insights from cations, silica and $\text{SO}_4\text{-H}_2\text{O}$ isotope geothermometers. *Appl Geochemistry*. 2020;113: 104492.
- Apollaro C, Caracausi A, Paternoster M, Randazzo P, Aiuppa A, De Rosa R, Fuoco I, Mongelli G, Muto F, Vanni E, Vespasiano G. Fluid geochemistry in a low-enthalpy geothermal field along a sector of southern Apennines chain (Italy). *J Geochem Explor*. 2020;219: 106618.
- Barde-Cabusson S, Finizola A, Revil A, Ricci T, Piscitelli S, Rizzo E, Angeletti B, Balasco M, Bennati L, Byrdina S, Carzaniga N, Crespy A, Di Gangi F, Morin J, Perrone A, Rossi M, Rouleau E, Suski B, Villeneuve N. New geological insights and structural control on fluid circulation in La Fossa cone (Vulcano, Aeolian Islands, Italy). *J Volcanol Geotherm Res*. 2009;185:231–45.
- Bowers TS, Jackson KJ, Helgeson HC. *Equilibrium Activity Diagrams for Coexisting Minerals and Aqueous Solutions at Pressures and Temperatures to 5 kb and 600°C*. Springer, 1984; 397 pp.
- Bucher K, Stober I. Fluids in the upper continental crust. *Geofluids*. 2010;10:241–53.
- Chen H, You W, Xiao Q. Thermal regime and paleogeothermal gradient evolution of Mesozoic-Cenozoic sedimentary basins in the Tibetan Plateau, China. *Earth Sci China Univ Geosci*. 2013;38:541–52.
- Clark ID, Fritz P. *Environmental isotopes in hydrology*. Boca Raton: CRC Press; 1997.
- Cortecci G, Boschetti T, Mussi M, Lameli CH, Mucchino C, Barbieri M. New chemical and original isotopic data on waters from El Tatio geothermal field, northern Chile. *Geochem J*. 2005;39:547–71.
- Craig H. Isotopic variations in meteoric waters. *Science*. 1961;133:1702–3.
- Drüppel K, Stober I, Grimmer JC, Mertz-Kraus R. Experimental alteration of granitic rocks: implications for the evolution of geothermal brines in the Upper Rhine Graben, Germany. *Geothermics*. 2020;88: 101903.
- Egger AE, Glen JMG, McPhee DK. Structural controls on geothermal circulation in Surprise Valley, California: a re-evaluation of the Lake City fault zone. *GSA Bull*. 2014;126:523–31.
- Fan Y, Zhang J, Lin C, Wang X, Zhang B. Miocene granitic magmatism constrains the early E-W extension in the Himalayan Orogen: a case study of Kung Co leucogranite. *Lithos*. 2021;398–399: 106295.
- Fournier RO. Chemical geothermometers and mixing models for geothermal systems. *Geothermics*. 1977;5:41–50.
- Fournier RO, Truesdell AH. An empirical Na–K–Ca geothermometer for natural waters. *Geochim Cosmochim Acta*. 1973;37:1255–75.
- Giggenbach WF. Geothermal solute equilibria. Derivation of Na–K–Mg–Ca geothermometers. *Geochim Cosmochim Acta*. 1988;52:2749–65.
- Giggenbach WF. Chemical techniques in geothermal exploration. In: D'Amore F, editor. *Applications of geochemistry in geothermal reservoir development: series of technical guides on the use of geothermal energy*. Rome: UNITAR/UNDP Centre on Small Energy Resources; 1991. p. 119–44.
- Giggenbach WF, Soto RC. Isotopic and chemical composition of water and steam discharges from volcanic–magmatic–hydrothermal systems of the Guanacaste Geothermal Province, Costa Rica. *Appl Geochem*. 1992;7:309–32.
- Goguel R. The rare alkalies in hydrothermal alteration at Wairakei and Broadlands, geothermal fields, N.Z. *Geochim Cosmochim Acta*. 1983;47:429–37.
- Guo Z, Wilson M, Zhang M, Cheng Z, Zhang L. Post-collisional, K-rich mafic magmatism in south Tibet: constraints on Indian slab-to-wedge transport processes and plateau uplift. *Contrib Mineral Petrol*. 2013;165:1311–40.
- Guo Z, Wilson M, Zhang M, Cheng Z, Zhang L. Post-collisional ultrapotassic mafic magmatism in South Tibet: products of partial melting of pyroxenite in the mantle wedge induced by roll-back and delamination of the subducted Indian continental lithosphere slab. *J Petrol*. 2015;56:1365–406.
- Hodges KV. Tectonics of the Himalaya and southern Tibet from two perspectives. *GSA Bull*. 2000;112:324–50.
- Isaji R, Okano O, Ohtani T, Takagi E, Sugihara Y, Ueda A. Sr isotope geochemical study of geothermal water and rocks from a newly drilled well for geothermal power generation and hot spring waters in the Okuhida Hot Spring, Gifu, Japan. *Geothermics*. 2021;91: 102018.
- Jácome-Paz MP, Pérez-Zarate D, Prol-Ledesma RM, Irving GR, Rodríguez A. Geochemical exploration in Mesillas geothermal area, Mexico. *Appl Geochem*. 2022;143: 105376.
- Jiang G, Hu S, Shi Y, Zhang C, Wang Z, Hu D. Terrestrial heat flow of continental China: Updated dataset and tectonic implications. *Tectonophysics*. 2019;753:36–48.
- Kaasalainen H, Stefánsson A. The chemistry of trace elements in surface geothermal waters and steam. *Iceland Chem Geol*. 2012;330–331:60–85.
- Kapp P, Decelles P. Mesozoic-Cenozoic geological evolution of the Himalayan-Tibetan orogen and working tectonic hypotheses. *Am J Sci*. 2019;319:159–254.
- Klemperer S, Zhao P, Whyte C, Darrah T, Crossey L, Karlstrom K, Liu T, Winn C, Hilton D, Ding L. Limited underthrusting of India below Tibet: $^3\text{He}/^4\text{He}$ analysis of thermal springs locates the mantle suture in continental collision. *Proc Natl Acad Sci*. 2022;119: e2113877119.
- Li H, Guo N, Sun H. Analysis of the hydrochemical characteristics of the Chazi thermal spring in Tibet. *Geol Rev*. 2019;65:3–4.
- Li X, Huang X, Liao X, Zhang Y-H. Hydrogeochemical characteristics and conceptual model of the geothermal waters in the xianshuihe fault zone, southwestern China. *Int J Environ Res Public Health*. 2020;17:50.
- Liu W, Guan L, Liu Y, Xie X, Zhang M, Chen B, Xu S, Sano Y. Fluid geochemistry and geothermal anomaly along the Yushu-Ganzi-Xianshuihe fault system, eastern Tibetan Plateau: implications for regional seismic activity. *J Hydrol*. 2022;607: 127554.
- Liu W, Zhang M, Liu Y, Cui L, Sano Y, Zhou X, Li Y, Zhang L, Lang Y-C, Liu C-Q, Xu S. Massive crustal carbon mobilization and emission driven by India underthrusting Asia. *Commun Earth Environ*. 2024;5:271.
- Luo J, Pang Z, Kong Y, Wang Y. Geothermal potential evaluation and development prioritization based on geochemistry of geothermal waters from Kangding area, western Sichuan, China. *Environ Earth Sci*. 2017;76:343.
- Mao Q, Zou G-F, Gu X-M, Chen L. Geochemical features and tectonic setting of granites in Gangba-dingri area of Southern Tibet. *Mineral Petrol*. 2012;39:67–77.

- Munoz-Saez C, Perez-Nuñez C, Martini S, Vargas-Barrera A, Reich M, Morata D, Manga M. The Alpehue geyser field, Solipulli Volcano, Chile. *J Volcanol Geotherm Res.* 2020;406:107065.
- Nábélek J, Hetényi G, Vergne J, Sapkota S, Kafle B, Jiang M, Su H, Chen J, Huang B-S. Underplating in the Himalaya-Tibet Collision Zone Revealed by the Hi-CLIMB experiment. *Science.* 2009;325:1371.
- Négrel P, Roy S. Chemistry of rainwater in the Massif Central (France): a strontium isotope and major Element Study. *Appl Geochem.* 1998;13:941–52.
- Negri A, Daniele L, Aravena D, Muñoz M, Delgado A, Morata D. Decoding fjord water contribution and geochemical processes in the Aysen thermal springs (Southern Patagonia, Chile). *J Geochemical Explor.* 2018;185:1–13.
- Newell DL, Jessup MJ, Cottle JM, Hilton DR, Sharp ZD, Fischer TP. Aqueous and isotope geochemistry of mineral springs along the southern margin of the Tibetan plateau: Implications for fluid sources and regional degassing of CO₂. *Geochem Geophys Geosyst.* 2008;9:Q08014.
- Notsu K, Wakita H, Nakamura Y. Strontium isotopic composition of hot spring and mineral spring waters, Japan. *Appl Geochem.* 1991;6:543–51.
- Öztekin Okan Ö, Kalender L, Çetindağ B. Trace-element hydrogeochemistry of thermal waters of Karakoçan (Elazığ) and Mazgirt (Tunceli), Eastern Anatolia, Turkey. *J Geochem Explor.* 2018;194:29–43.
- Palmer MR, Edmond JM. Controls over the strontium isotope composition of river water. *Geochim Cosmochim Acta.* 1992;56:2099–111.
- Pang ZH, Reed M. Theoretical chemical thermometry on geothermal waters: problems and methods. *Geochem Cosmochim Acta.* 1998;6:1083–91.
- Pantić TP, Birke M, Petrović B, Nikolov J, Dragišić V, Živanović V. Hydrogeochemistry of thermal groundwaters in the Serbian crystalline core region. *J Geochem Explor.* 2015;159:101–14.
- Parkhurst DL, Appelo CAJ. Description of input and examples for PHREEQC version 3: a computer program for speciation, batch-reaction, one-dimensional transport, and inverse geochemical calculations. U.S. Geological Survey Techniques and Methods Techniques and Methods (497pp). 2013.
- Parsons AJ, Hosseini K, Palin RM, Sigloch K. Geological, geophysical and plate kinematic constraints for models of the India-Asia collision and the post-Triassic central Tethys oceans. *Earth-Sci Rev.* 2020;208: 103084.
- Pérez-Zárate D, Prol-Ledesma RM, Rodríguez-Díaz AA, Jácome-Paz MP, González-Romo IA. Soil gas flux, hydrogeochemistry and multicomponent geothermometry of thermal springs in the La Escalera geothermal prospect, Mexico. *Appl Geochem.* 2022;139: 105256.
- Reyes AG, Trompette WJ. Hydrothermal water–rock interaction and the redistribution of Li, B and Cl in the Taupo Volcanic Zone, New Zealand. *Chem Geol.* 2012;314–317:96–112.
- Rowland JC, Manga M, Rose TP. The influence of poorly interconnected fault zone flow paths on spring geochemistry. *Geofluids.* 2008;8:93–101.
- Scott BE, Newell DL, Jessup MJ, Grambling TA, Shaw CA. Structural controls on crustal fluid circulation and hot spring geochemistry above a flat-slab subduction zone, Peru. *Geochem Geophys Geosyst.* 2020;21:e2020GC008919.
- Shakeri A, Moore F, Kompani-Zare M. Geochemistry of the thermal springs of Mount Taftan, southeastern Iran. *J Volcanol Geotherm Res.* 2008;178:829–36.
- Shaw DM, Sturchio NC. Boron–lithium relationships in rhyolites and associated thermal waters of young silicic calderas, with comments on incompatible element behaviour. *Geochim Cosmochim Acta.* 1992;56:3723–31.
- Sorey ML, Lewis ER. Convective heat flow from hot springs in the Long Valley Caldera, Mono County, California. *J Geophys Res Space Phys.* 1976;81:785–91.
- Spycher N, Peiffer L, Sonnenthal EL, Saldi G, Reed MH, Kennedy BM. Integrated multicomponent solute geothermometry. *Geothermics.* 2014;51:113–23.
- Spycher N, Peiffer L, Finsterle S, Sonnenthal E. *GeoT User's Guide, a Computer Program for Multicomponent Geothermometry and Geochemical Speciation Version 2.1.* 2016.
- Stober I, Zhong J, Zhang L, Bucher K. Deep hydrothermal fluid–rock interaction: the thermal springs of Da Qaidam, China. *Geofluids.* 2016;16:711–28.
- Sundell KE, Taylor MH, Styron RH, Stockli DF, Kapp P, Hager C, Liu D, Ding L. Evidence for constriction and Pliocene acceleration of east–west extension in the North Lunggar rift region of west central Tibet. *Tectonics.* 2013;32:1454–79.
- Tan H, Zhang Y, Zhang W, Kong N, Zhang Q, Huang J. Understanding the circulation of geothermal waters in the Tibetan Plateau using oxygen and hydrogen stable isotopes. *Appl Geochemistry.* 2014;51:23–32.
- Tardani D, Roulleau E, Pinti DL, Pérez-Flores P, Daniele L, Reich M, Sanchez-Alfaro P, Morata D, Richard L. Structural control on shallow hydrogeochemical processes at Caviahue-Copahue Volcanic Complex (CCVC), Argentina. *J Volcanol Geotherm Res.* 2021;414: 107228.
- Tong W, Liao Z, Liu S, Zhang Z, You M, Zhang M. *Thermal Springs in Tibet.* Beijing, China: Science Press; 2000.
- Truesdell AH, Fournier RO. Procedure for estimating the temperature of a hot water component in a mixed water using a plot of dissolved silica versus enthalpy. *J Res U S Geol Surv.* 1977;5(1):49–52.
- Unsworth MJ, Jones AG, Wei W, Marquis G, Gokarn SG, Spratt JE, Bedrosian P, Booker J, Leshou C, Clarke G, Shenghui L, Chanhong L, Ming D, Sheng J, Solon K, Handong T, Ledo J, Roberts B. Crustal rheology of the Himalaya and Southern Tibet inferred from magnetotelluric data. *Nature.* 2005;438:78–81.
- van Hinsbergen DJJ, Lippert PC, Li S, Huang W, Advokaat EL, Spakman W. Reconstructing Greater India: paleogeographic, kinematic, and geodynamic perspectives. *Tectonophysics.* 2019;760:69–94.
- Verma SP, Santoyo E. New improved equations for Na/K, Na/Li and SiO₂ geothermometers by outlier detection and rejection. *J Volcanol Geoth Res.* 1997;79:9–24.
- Wang Q, Zhu D-C, Cawood PA, Zhao Z-D, Liu S-A, Chung S-L, Zhang L-L, Liu D, Zheng Y-C, Dai J-G. Eocene magmatic processes and crustal thickening in southern Tibet: insights from strongly fractionated ca. 43Ma granites in the western Gangdese Batholith. *Lithos.* 2015;239:128–41.
- Wang S, Lu C, Nan D, Hu X, Shao J. Geothermal resources in Tibet of China: current status and prospective development. *Environ Earth Sci.* 2017;76:239.

- Wang C, Zheng M, Zhang X, Xing E, Zhang J, Ren J, Ling Y, O, H, and Sr isotope evidence for origin and mixing processes of the Gudui geothermal system, Himalayas, China. *Geosci Front.* 2020;11:1175–87.
- Wang Y, Li L, Wen H, Hao Y. Geochemical evidence for the nonexistence of supercritical geothermal fluids at the Yangbajing geothermal field, southern Tibet. *J Hydrol.* 2022;604: 127243.
- Yin A, Harrison TM. Geologic evolution of the Himalayan-Tibetan orogen. *Annu Rev Earth Planet Sci Lett.* 2000;28:211–80.
- Yu J, Zhang H, Yu F, Liu D. Oxygen and hydrogen isotopic compositions of meteoric waters in the eastern part of Xizang. *Geochemistry.* 1984;3:93–101.
- Yuan J, Guo Q, Wang Y. Geochemical behaviors of boron and its isotopes in aqueous environment of the Yangbajing and Yangyi geothermal fields, Tibet, China. *J Geochem Explor.* 2014;140:11–22.
- Zhang M, Zhang L, Zhao W, Guo Z, Xu S, Sano Y, Lang YC, Liu CQ, Li Y. Metamorphic CO₂ emissions from the southern Yadong-Gulu rift, Tibetan Plateau: insights into deep carbon cycle in the India-Asia continental collision zone. *Chem Geol.* 2021;584: 120534.
- Zhao P, Dor J, Liang T, Jin J, Zhang H. Characteristics of gas geochemistry in Yangbajing geothermal field, Tibet. *Chin Sci Bull.* 1998;43:1770–7.
- Zhao W, Guo Z, Zheng G, Pinti DL, Zhang M, Li J, Ma L. Subducting Indian lithosphere controls the deep carbon emission in Lhasa terrane, southern Tibet. *J Geophys Res Solid Earth.* 2022;127:e2022JB024250.
- Zhou H, Kuang X, Hao Y, Wang C, Feng Y, Zou Y, Zhu M, Zheng C. Magmatic fluid input controlling the geochemical and isotopic characteristics of geothermal waters along the Yadong-Gulu rift, southern Tibetan Plateau. *J Hydrol.* 2023;619: 129196.

Publisher's Note

Springer Nature remains neutral with regard to jurisdictional claims in published maps and institutional affiliations.